

## A NEW NON-PLANETARY INTERPRETATION OF THE MICROLENSING EVENT OGLE-2013-BLG-0723

CHEONGHO HAN<sup>1</sup>, DAVID P. BENNETT<sup>2,3</sup>, ANDRZEJ UDALSKI<sup>4</sup>, AND YOUN KIL JUNG<sup>1</sup>

<sup>1</sup>Department of Physics, Institute for Astrophysics, Chungbuk National University, 371-763 Cheongju, Republic of Korea,

<sup>2</sup>Code 667, NASA Goddard Space Flight Center, Greenbelt, MD 20771, USA

<sup>3</sup>University of Notre Dame, Department of Physics, 225 Nieuwland Science Hall, Notre Dame, IN 46556-5670, USA,

<sup>4</sup>Warsaw University Observatory, Al. Ujazdowskie 4, 00-478 Warszawa, Poland

*Draft version October 8, 2018*

### ABSTRACT

Recently, the discovery of a Venus-mass planet orbiting a brown-dwarf host in a binary system was reported from the analysis of the microlensing event OGLE-2013-BLG-0723. We reanalyze the event considering the possibility of other interpretations. From this, we find a new solution where the lens is composed of 2 bodies in contrast to the 3-body solution of the previous analysis. The new solution better explains the observed light curve than the previous solution with  $\Delta\chi^2 \sim 202$ , suggesting that the new solution is a correct model for the event. From the estimation of the physical parameters based on the new interpretation, we find that the lens system is composed of two low-mass stars with  $\sim 0.2 M_\odot$  and  $\sim 0.1 M_\odot$  and located at a distance  $\sim 3$  kpc. The fact that the physical parameters correspond to those of the most common lens population located at a distance with a large lensing probability further supports the likelihood of the new interpretation. Considering that two dramatically different solutions can approximately explain the observed light curve, the event suggests the need of carefully testing all possible lens-system geometries.

*Subject headings:* gravitational lensing: micro – planetary systems

### 1. INTRODUCTION

Recently, the microlensing discovery of a Venus-mass planet (OGLE-2013-BLG-0723LBb) orbiting a brown dwarf in a binary system was reported by Udalski et al. (2015). The discovery of the planet was of special scientific interest in many aspects. First, the planet itself is the lowest-mass planet among those discovered by using the microlensing method. Second, the host of the planet is a substellar-mass brown dwarf suggesting the possibility that an ice-rock planets can be formed in the outer parts of the accretion disk around a brown dwarf. Third, the planet belongs to a binary system where the planet orbits the lower-mass component of the binary. Finally, the planet/host mass ratio indicates that the system may be viewed either as a scaled-down version of a planet plus a star or as a scaled-up version of a moon plus a planet orbiting a star, suggesting that the formation processes of companions within accretion disks around stars, brown dwarfs, and planets are similar.

The light curve of the microlensing event OGLE-2013-BLG-0723 is complex and composed of multiple anomalous features. See the light curve in Figure 1. In chronological order, there exists a short-term anomaly occurred at  $\text{HJD}' = \text{HJD} - 2450000 \sim 6424$  followed by a bump at  $\text{HJD}' \sim 6463$  and two sharp spikes occurred at  $\text{HJD}' \sim 6472$  and  $6492$ . According to the interpretation of Udalski et al. (2015), the main anomalous features (the bump and the two spikes) of the light curve were produced by a wide binary where the projected separation between the binary components is greater than the angular Einstein radius  $\theta_E$  of the lens system and the short-term anomaly was produced by a planetary-mass object accompanied to the lower-mass component of the binary. See the geometry of the lens system presented in Figure 2 of Udalski et al. (2015).

For lensing light curves produced by binary objects, it is known that there can be a pair of degenerate solutions where one solution has a binary separation normalized to the Ein-

stein radius,  $s$ , is greater than unity,  $s > 1$  (wide binary), and the other solution has a separation smaller than unity,  $s < 1$  (close binary) (Griest & Safizadeh 1998; Dominik 1999). According to the interpretation of Udalski et al. (2015), the main features of the light curve were explained by a wide-binary solution. They did find a close-binary solution<sup>1</sup>, but the solution was rejected because it resulted in unphysical lens parameters.

In this work, we present another interpretation of the lensing event OGLE-2013-BLG-0723 based on a new solution of lensing parameters found from the reanalysis of the event. According to this interpretation, all features of the lensing light curve including the short-term anomaly can be explained by a close-binary model, that was not found in the previous analysis, without the need to introduce an additional planet.

### 2. REANALYSIS

Microlensing light curves produced by binary objects are described by many parameters. For the simplest case of a rectilinear lens-source relative motion, one needs 7 basic parameters. Among these parameters, 3 parameters describe the relative lens-source motion, including the time of the closest source approach to a reference position of the lens,  $t_0$ , the separation between the source and the reference position at  $t_0$ ,  $u_0$  (normalized to the angular Einstein radius  $\theta_E$ ), and the angle between the source trajectory and the binary axis,  $\alpha$ . In our modeling, we use the barycenter of the binary as a reference position. The Einstein time scale  $t_E$ , which is defined as the time required for the source to cross the Einstein radius, is needed to characterize the time scale of an event. Another two parameters of the projected binary separation,  $s$  (also normalized to  $\theta_E$ ), and the mass ratio between the binary components,  $q$ , characterize the binary lens components. The last parameter is the normalized source radius  $\rho = \theta_*/\theta_E$ , where  $\theta_*$  is the angular source radius. This parameter is needed to describe the caustic-crossing features that are affected by

<sup>1</sup> This solution is different from that one presented in this work.

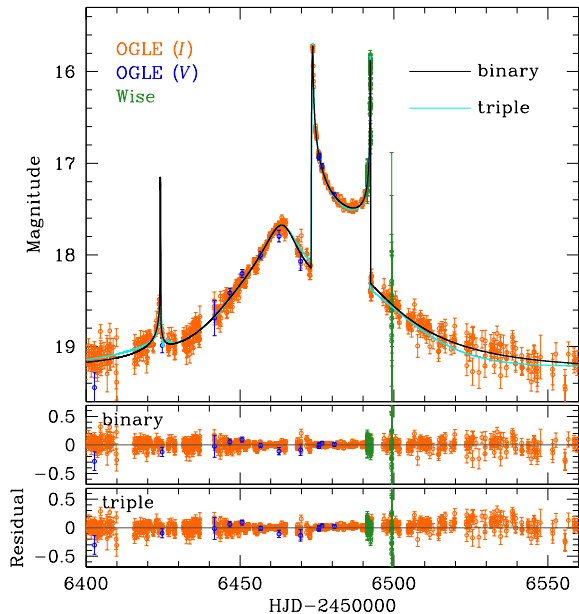


FIG. 1.— Light curve of OGLE-2013-BLG-0723. The cyan and black curves plotted over the data are the best-fit models obtained from the previous 3-body model and the newly found 2-body model, respectively. The two lower panels show the residuals from the individual models.

finite-source effects. See Figure 6 of Jung et al. (2015) for the graphical presentation of the binary lensing parameters.

Modeling based on the basic parameters is often not enough to precisely describe lensing light curves and additional parameters are needed to consider higher-order effects. In order to consider parallax effects, which are caused by the positional change of the observer induced by the orbital motion of the Earth around the Sun (Gould 1992), one needs two additional parameters  $\pi_{E,N}$  and  $\pi_{E,E}$ . These parameters represent the two components of the lens parallax vector  $\pi_E$  projected onto the sky along the north and east equatorial coordinates, respectively. The magnitude of the parallax vector corresponds to  $\pi_E = \pi_{\text{rel}}/\theta_E$ , where  $\pi_{\text{rel}} = \text{AU}(D_L^{-1} - D_S^{-1})$  is the relative lens-source parallax,  $D_L$  and  $D_S$  are the distances to the lens and source, respectively. The direction of  $\pi_E$  is that of the relative lens-source motion in the frame of the Earth at a reference time of the event.

Another higher-order effect that is often needed to consider in binary-lens modeling is the orbital motion of the lens (Park et al. 2013). To first-order approximation, the lens-orbital effect is described by two parameters  $ds/dt$  and  $d\alpha/dt$ , which represent the change rates of the binary separation and the source trajectory angle, respectively (Albrow et al. 2000).

Ideally, a solution of lensing parameters can be searched for by comparing an observed light curve with all possible model light curves resulting from the combination of lensing parameters. However, thorough coverage of the vast parameter space is limited by computing power and thus the grid spacing of each parameter cannot be arbitrarily small to completely cover the parameter space. As a result, solutions of lensing parameters, especially ones located in a very localized region in the parameter space, can be occasionally missed.<sup>2</sup>

The reanalysis of this event was initiated by one of us

<sup>2</sup> An adaptive mesh refinement approach, which locally adds more grids where they are needed, can help to minimize the probability of missing solutions, but such a code has not yet been developed in microlensing analysis due to the difficulty in providing a prior condition for denser grid regions.

(DPB) using the initial condition grid search method of Bennett (2010) with the data set used in the original paper (Udalski et al. 2015). To limit the parameter space to be searched, the initial search was conducted using only a stellar binary model without microlensing parallax or orbital motion. This search yielded a candidate solution with a caustic crossing feature at  $\text{HJD}' \approx 6414.5$  where there is a gap in the data. This is relatively close to the observed light curve bump at  $\text{HJD}' \approx 6424$ , suggesting that a model including parallax and/or orbital motion might naturally explain the light curve. Several similar models were explored, and a model including microlensing parallax with the early light curve peak at  $\text{HJD}' \approx 6424$  was found. This solution was sent to the lead authors of the original paper, while models also including orbital motion were investigated.

Considering the possibility that there may exist missed solutions, especially in the close binary regime, we conduct reanalysis of the lensing event OGLE-2013-BLG-0723. In this analysis, we narrow down the grid spacing of parameters in order to minimize the possibility of missing localized solutions. We also consider higher-order effects in the initial solution search to avoid the possibility that local solutions are missed due to the neglect of higher-order effects. The grid search is conducted in the space of the parameters  $(s, q, \alpha)$  because lensing light curves can change dramatically with the small changes of these parameters. To search for other parameters, for which lensing light curves vary smoothly with the change of the parameters, a downhill approach is used. For the downhill approach, we use a Markov Chain Monte Carlo (MCMC) method.

It is needed to consider finite-source effects in order to describe the caustic-crossing parts of the light curve. We incorporate the effects by using a numerical ray-shooting method. In this method, uniform rays are shot from the image plane, bent by the lens equation, and then collected in the source plane. Then, finite magnifications are computed as the ratio of the ray number density on the source plane to the density on the image plane. Since precise computations of finite magnifications require a large number of rays, this numerical method demands large amount of computing power. For efficient production of theoretical light curves, we apply the “map-making” method (Dong et al. 2006), where one can produce many light curves resulting from different source trajectories based on a single ray-shooting map for a given set of the binary parameters  $s$  and  $q$ . In computing finite-source magnifications, we consider the surface-brightness variation of the source star by modeling the surface-brightness profile as  $S_\lambda \propto 1 - \Gamma_\lambda(3 \cos \psi/2)$ , where  $\Gamma_\lambda$  is the linear limb-darkening coefficient  $\psi$  is the angle between the line of sight toward the source center and the normal to the surface. The limb-darkening coefficient  $\Gamma_l = 0.36$  is adopted from Claret (2000) based on the source type. For the detailed procedure of determining the source type, see section 4.

We note that it is difficult to consider lens-orbital effects in the initial search for solutions based on the map-making method. This is because the binary separation and orientation vary in time during events and thus a single map cannot be used to produce multiple light curves. We, therefore, consider orbital effects after a preliminary solution is found from the initial search.

For direct comparison of models, we use the same data sets as those used in Udalski et al. (2015). These data sets are composed of 4067 *I*-band and 19 *V*-band data acquired by the Optical Gravitational Lensing Experiment (OGLE) group and

TABLE 1  
 LENSING PARAMETERS

| Parameter                         | Standard             | Parallax             |                      | Orbital              | Orbital + Parallax   |                      |
|-----------------------------------|----------------------|----------------------|----------------------|----------------------|----------------------|----------------------|
|                                   |                      | $u_0 > 0$            | $u_0 < 0$            |                      | $u_0 > 0$            | $u_0 < 0$            |
| $\chi^2$                          | 5536.9               | 4292.3               | 4211.1               | 3936.2               | 3925.1               | 3930.1               |
| $t_0$ (HJD')                      | $6485.057 \pm 0.028$ | $6485.055 \pm 0.038$ | $6485.285 \pm 0.048$ | $6485.976 \pm 0.054$ | $6486.004 \pm 0.056$ | $6486.007 \pm 0.069$ |
| $u_0$                             | $0.0133 \pm 0.001$   | $0.019 \pm 0.002$    | $-0.013 \pm 0.001$   | $0.032 \pm 0.002$    | $0.030 \pm 0.001$    | $-0.028 \pm 0.001$   |
| $t_E$ (days)                      | $48.60 \pm 0.07$     | $55.24 \pm 0.22$     | $47.97 \pm 0.22$     | $51.93 \pm 0.42$     | $50.65 \pm 0.52$     | $51.33 \pm 0.48$     |
| $s$                               | $0.668 \pm 0.001$    | $0.670 \pm 0.001$    | $0.665 \pm 0.001$    | $0.672 \pm 0.003$    | $0.672 \pm 0.003$    | $0.666 \pm 0.003$    |
| $q$                               | $0.585 \pm 0.003$    | $0.411 \pm 0.005$    | $0.562 \pm 0.009$    | $0.529 \pm 0.007$    | $0.562 \pm 0.011$    | $0.560 \pm 0.011$    |
| $\alpha$ (rad)                    | $4.892 \pm 0.002$    | $-4.939 \pm 0.005$   | $4.879 \pm 0.004$    | $-4.991 \pm 0.005$   | $-4.975 \pm 0.007$   | $4.963 \pm 0.005$    |
| $\rho$ ( $10^{-3}$ )              | $1.04 \pm 0.01$      | $1.08 \pm 0.02$      | $1.06 \pm 0.02$      | $1.19 \pm 0.02$      | $1.19 \pm 0.02$      | $1.16 \pm 0.02$      |
| $\pi_{E,N}$                       | -                    | $-1.14 \pm 0.04$     | $0.70 \pm 0.04$      | -                    | $0.05 \pm 0.04$      | $0.10 \pm 0.07$      |
| $\pi_{E,E}$                       | -                    | $0.04 \pm 0.05$      | $1.15 \pm 0.09$      | -                    | $0.26 \pm 0.07$      | $0.30 \pm 0.08$      |
| $ds/dt$ ( $\text{yr}^{-1}$ )      | -                    | -                    | -                    | $0.06 \pm 0.04$      | $0.08 \pm 0.04$      | $-0.01 \pm 0.03$     |
| $d\alpha/dt$ ( $\text{yr}^{-1}$ ) | -                    | -                    | -                    | $-0.46 \pm 0.03$     | $-0.53 \pm 0.03$     | $0.44 \pm 0.03$      |

NOTE. — HJD' = HJD - 2450000.

 TABLE 2  
 Lensing parameters of 3-body model

| Quantity                        | Value                |
|---------------------------------|----------------------|
| $\chi^2$                        | 4126.8               |
| $t_0$ (HJD')                    | $6484.526 \pm 0.037$ |
| $u_0$                           | $-0.079 \pm 0.002$   |
| $t_E$ (days)                    | $68.48 \pm 0.01$     |
| $s_1$                           | $5.07 \pm 0.02$      |
| $q_1$                           | $3.11 \pm 0.02$      |
| $\alpha$ (rad)                  | $-1.195 \pm 0.003$   |
| $s_2$                           | $0.97 \pm 0.02$      |
| $q_2$ ( $10^{-5}$ )             | $6.61 \pm 0.01$      |
| $\psi_0$ (rad)                  | $-4.936 \pm 0.005$   |
| $\rho$ ( $10^{-3}$ )            | $1.40 \pm 0.02$      |
| $\pi_{E,N}$                     | $-0.05 \pm 0.01$     |
| $\pi_{E,E}$                     | $1.35 \pm 0.02$      |
| $ds_2/dt$ ( $\text{yr}^{-1}$ )  | $0.81 \pm 0.02$      |
| $d\psi/dt$ ( $\text{yr}^{-1}$ ) | $-0.50 \pm 0.02$     |

62 *I*-band data obtained by the Wise group. We also use the same error-bar normalization. Since  $\chi^2$  per degree of freedom is normalized to unity,  $\Delta\chi^2 = n^2$  corresponds to the statistical importance of  $n\sigma$  level.

### 3. NEW INTERPRETATION

From the grid search, we find a new candidate close-binary solution that was not found in the previous analysis. It turns out that the new solution was missed because the grid spacing was not small enough to locate the isolated solution in the parameter space. Once the approximate region of the solution in the parameter space is located, we gradually refine the solution first by allowing grid parameters to vary and then by considering higher-order effects.

Based on the newly found local minima, we test 5 different models. In the “standard” binary-lens model, we model the light curve based on the 7 basic lensing parameters. In the “parallax” and “orbital” models, we separately consider the lens parallax and orbital effects, respectively. In the “orbital + parallax” model, we consider both lens-orbital motion and parallax effects. In order to check the well-known “ecliptic degeneracy” in the determination of the lens parallax (Skowron et al. 2011), we test two models with  $u_0 > 0$  and  $u_0 < 0$  for models considering parallax effects.

In Table 1, we present the best-fit parameters of the individual tested models along with their  $\chi^2$  values. In Table 2, we also present the parameters of the best-fit 3-body solution of Udalski et al. (2015) for comparison. We note that notations

of the 3-body lensing parameters are different from those of the 2-body parameters due to the addition of one more lens component. For example,  $(s_1, q_1)$  and  $(s_2, q_2)$  denote the separations and mass ratios between  $M_1 - M_2$  and  $M_1 - M_3$  pairs, respectively, and  $M_1, M_2$ , and  $M_3$  denote the lens components according to the order of heavier mass. The notation  $\psi_0$  denotes the angle between the binary axis and the planet-host axis at  $t_0$  and  $ds_2/dt$  and  $d\psi/dt$  are the change rates of  $s_2$  and  $\psi$ , respectively.

We find that higher-order effects are important for the precise description of the event. It is found that the standard model with  $\chi^2 = 5536.9$  cannot explain the short-term anomaly. Furthermore, it leaves noticeable residuals in the regions of the light curve around the other anomalous features. Consideration of the higher-order effects significantly improves the fit. We find that inclusion of parallax effects improves the fit by  $\Delta\chi^2 = 1326$ . The improvement by considering lens-orbital effects is  $\Delta\chi^2 = 1601$ . When both higher-order effects are simultaneously considered, the improvement is  $\Delta\chi^2 = 1612$ . Considering that (1)  $\chi^2$  improvement by the orbital effect is significantly greater than the improvement by the parallax effect and (2) the additional improvement from the orbital model to the orbital + parallax model is minor ( $\Delta\chi^2 = 11$ ), we judge that the lens orbital motion is the dominant higher-order effect. With the inclusion of the higher-order effects, the lensing light curve fits all anomalous features.

In Figure 1, we present the light curve of the close-binary model obtained from the reanalysis. For comparison, we also present the triple-lens model light curve that is constructed based on the best-fit parameters presented in Udalski et al. (2015). Figure 2 shows the lens-system geometry of the close binary model where the source trajectory with respect to the caustics are presented. According to the new close-binary model, the short-term anomaly was produced by the passage of the source over the tip of the 3-cusp peripheral caustic, and the two caustic-crossing spikes were produced by the source passage over the 4-cusp central caustic. The bump between the short-term anomaly and the caustic-crossing spikes was produced when the source passed over the narrow strip of the strong anomaly region formed along the line connecting the sharp cusps of the central and peripheral caustics. In Figure 3, we also present the distribution of the lensing parameters of the best-fit solution.

We find that both the previous 3-body and the new 2-body

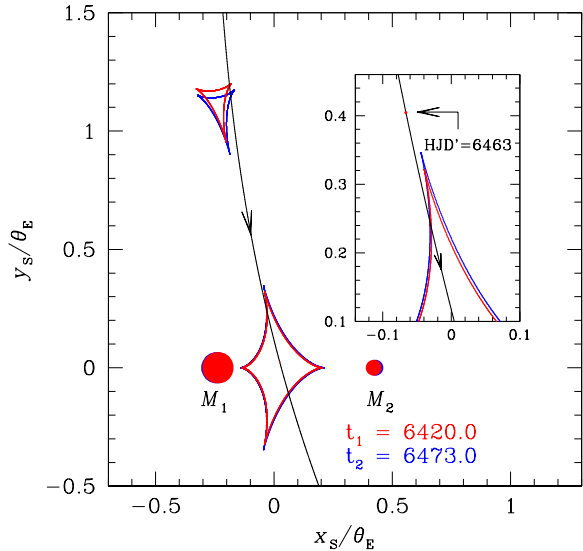


FIG. 2.— Geometry of the lens system. The closed curves with cusps are the caustics of the lens and the curve with an arrow is the source trajectory. The two filled dots marked by  $M_1$  and  $M_2$  are the positions of the binary lens components. All lengths are normalized to the angular Einstein radius  $\theta_E$  and the coordinates are centered at the barycenter of the binary lens. The inset shows the zoom of the region around the upper sharp cusp of the central caustic. The very tiny circle marked by  $\text{HJD}' = 6463$  represents the source position at the time of the bump located between the short-term anomaly and the caustic-crossing spikes in the lensing light curve. The size of the circle represents the source size scaled to the caustic size. Due to the orbital motion of the binary lens, the positions of the lens components and the corresponding caustics vary in time. We present the positions of the lens and caustics at two different epochs  $\text{HJD}' = 6420$  and  $6473$ , which correspond to the time of the short-term anomaly and the first source star's crossing of the central caustic, respectively.

solutions almost equally well explain the short-term anomaly. In Figure 4, we present the enlargement of the anomaly region over which we plot both model light curves. The lower panel shows the  $\chi^2$  difference between the two models. Positive  $\Delta\chi^2$  value means that the binary model provides a better fit and vice versa. One finds that  $\chi^2$  difference for nearly all data points are  $\lesssim 1$ , implying that the anomaly is well explained by both solutions. We note that despite the almost the same goodness of the fits, the two models are greatly different; the binary solution predicts a huge 1.5 – 2.0 mag brightening, while the triple model predicts a mild variation. If there existed a few points at the peak of the anomaly, the two models could have been clearly distinguished. Unfortunately, this part of the light curve was not covered by data.

Although it is difficult to resolve the degeneracy between the two solutions based on the short anomaly, we find that the degeneracy can be resolved from the overall light curve. One can see the goodness of the 2-body fit over the 3-body fit from the comparison of  $\chi^2$  values of the fits presented in Tables 1 and 2 and the cumulative function of  $\Delta\chi^2$  between the two models as a function of time presented in Figure 5. It is found that the 2-body solution with  $\chi^2 = 3925.1$  provides a better fit over the 3-body solution with  $\chi^2 = 4126.8$ , i.e.  $\Delta\chi^2 = 201.7$ . From the cumulative distribution, it is found that the 2-body solution better explains the observed light curve in the regions between the caustic crossings and the declining part of the light curve after the caustic crossings. We find that the  $\chi^2$  difference between the two models is  $\Delta\chi^2 = 202$ . We note that  $\chi^2 \sim 50$  improvement is achieved

during  $6510 \lesssim \text{HJD}' \lesssim 6540$ , when the phase of the Moon was close to full and thus data show somewhat larger scatter. We note, however, that the fit improvement is not attributed to the effect of elevated sky background or other noise because such an effect was accounted for in the error bar estimation during photometry procedure. Furthermore, the sharp increases in the cumulative  $\chi^2$  plot in other regions, especially around the caustic-crossing regions, demonstrate the better fit of the new solution. Udalski et al. (2015) mentioned a systematic trend in the baseline magnitude of the source star caused by a nearby bright star. In Appendix, we show this trend. We also describe the procedure to correct the systematic trend. We note that the improvement of the fit by the new solution is not attributed to this systematic trend because we use data set where the trend was corrected. Considering that not only the new solution provides a better fit but also the 2-body model is simpler than the 3-body model, the 2-body solution is likely to be the correct solution according to Occam's razor.

We consider two tests that may further support our new interpretation. The first test is checking the brightnesses of the source and blend predicted by the two models from high-resolution observations. We find that this method would not work because the estimated source and blend fluxes of the binary solution  $(F_s, F_b) = (0.151 \pm 0.001, 0.170 \pm 0.001)$  are not much different from  $(F_s, F_b) = (0.191 \pm 0.001, 0.132 \pm 0.001)$  of the triple-lens solution. The second test is measuring the relative lens-source proper motion. The detailed procedure of computing the proper motion is described in the next section. We find that the heliocentric proper motion estimated from the binary model is  $\mu_\odot = 6.4 \pm 0.5 \text{ mas yr}^{-1}$ , while the expected value for the triple-lens model is  $\mu_\odot = 14.5 \pm 1.3 \text{ mas yr}^{-1}$ . The difference between the estimated proper motions is considerable, implying that future observations with high-resolution instrument will be able to distinguish the two solutions.

In the aspect that there exist multiple interpretations for an isolated short-term anomaly located away from the main light curve, OGLE-2013-BLG-0723 is similar to the case of MACHO-97-BLG-41. For MACHO-97-BLG-41, there existed two interpretations: one interpretation by a 3-body circumbinary planetary system (Bennett et al. 1999) and the other by a 2-body orbiting binary system (Albrow et al. 2000; Jung et al. 2013). Considering that two solutions with dramatically different lens systems can explain observed light curves, the two events suggest the need of carefully testing all possible lens-system geometries.

#### 4. NEW ESTIMATION OF PHYSICAL PARAMETERS

For the new solution, both finite-source and parallax effects are detected and thus we are able to determine the angular Einstein radius  $\theta_E$  and the lens parallax  $\pi_E$ . With these values, the mass and distance to the lens are uniquely determined by

$$M_{\text{tot}} = \frac{\theta_E}{\kappa\pi_E}; \quad D_L = \frac{\text{AU}}{\pi_E\theta_E + \pi_S}, \quad (1)$$

where  $\kappa = 4G/(c^2\text{AU})$  and  $\pi_S = \text{AU}/D_S$  is the parallax of the source star (Gould 2000). The lens parallax is determined from modeling. The angular Einstein radius is estimated from the relation  $\theta_E = \theta_*/\rho$ , where the normalized source radius  $\rho$  is measured from modeling and the angular source radius  $\theta_*$  is estimated from the source type that is determined based on the de-reddened color and brightness. For the calibration of the color and brightness of the source star, we use the cen-

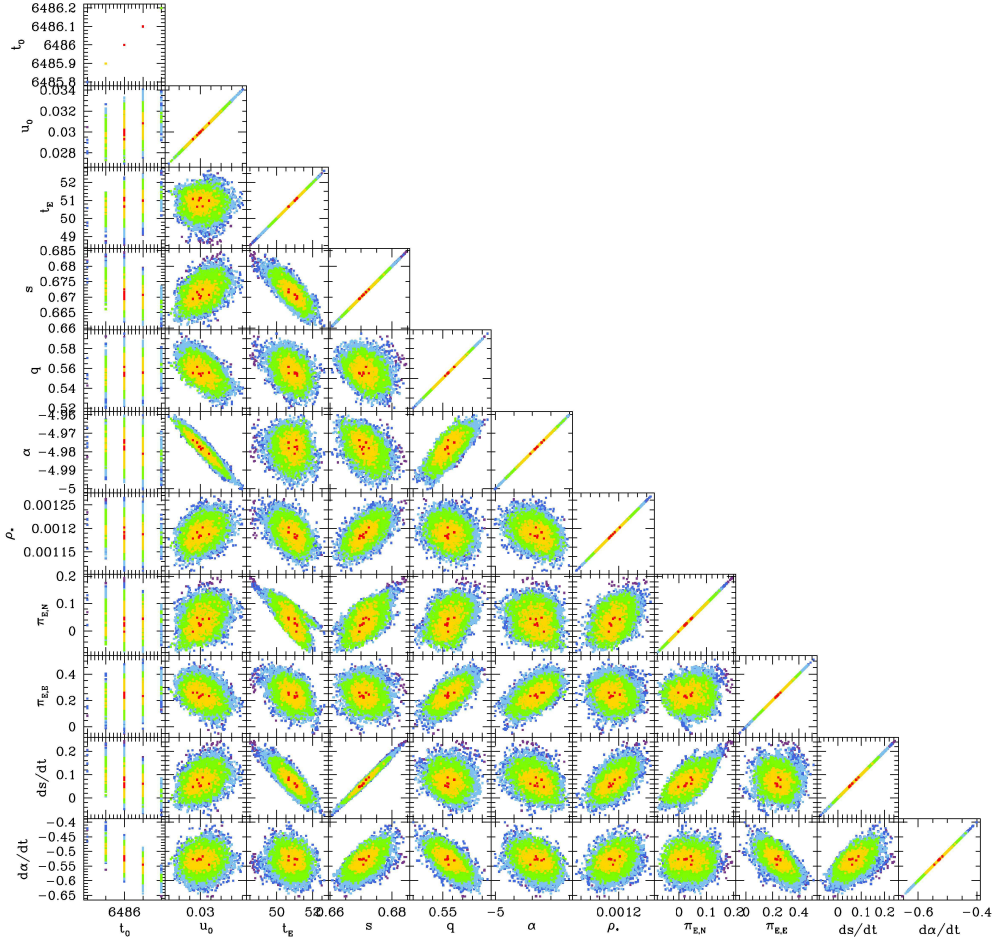


FIG. 3.— Distribution of the lensing parameters of the newly found binary solution. The color coding represents points on the MCMC chain within 1 (red), 2 (yellow), 3 (green), 4 (cyan), 5 (blue)  $\sigma$  of the best fit.

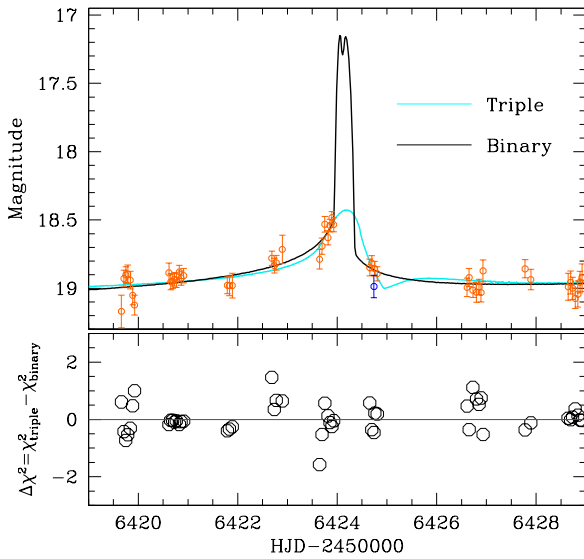


FIG. 4.— Enlargement of the light curve near the short-term anomaly around  $\text{HJD}' \sim 6424$ . The lower panel shows the  $\chi^2$  difference between the new binary and previous triple-lens solutions. Positive  $\Delta\chi^2$  implies that the 2-body model provides a better fit and vice versa.

trold of bulge giant clump as a reference (Yoo et al. 2004). In Figure 6, we present the position of the source with respect to the centroid of the giant clump in the color-magnitude diagram. The estimated de-reddened color and brightness of the source star are  $(V-I, I)_0 = (0.52 \pm 0.05, 17.3 \pm 0.01)$ , indicating that the source is an F-type main-sequence star. We then convert  $V-I$  color into  $V-K$  color using the color-color relation of Bessell & Brett (1988) and obtain the angular source radius  $\theta_*$  using the relation between  $V-K$  and  $\theta_*$  presented in Kervella et al. (2004). The estimated source radius is  $\theta_* = 0.90 \pm 0.06 \mu\text{as}$ . We note that the source radius is slightly smaller than the value estimated in Udalski et al. (2015) because of the slight color difference, which is caused by the difference in the ratios of the source to blended light between the two models. From the angular source radius, the estimated the angular Einstein radius is  $\theta_E = 0.75 \pm 0.05 \text{ mas}$ .

In Table 3, we list the determined physical parameters. Although the  $u_0 > 0$  solution is slightly preferred over the  $u_0 < 0$  solution, it is found that the  $\chi^2$  difference between the two models is merely  $\Delta\chi^2 = 5.0$ . Since such a level of  $\Delta\chi^2$  can be ascribed to systematics in data, we present the physical parameters corresponding to both solutions. We note, however, that the estimated lens parallax values from the two models are similar each other and thus the resulting physical parameters are also similar. Once the distance to the lens is known,

TABLE 3  
PHYSICAL LENS PARAMETERS

| Parameter  | $u_0 > 0$                            | $u_0 < 0$                            |
|--|--------------------------------------|--------------------------------------|
| Primary mass                                       | $0.22 \pm 0.06 M_\odot$              | $0.19 \pm 0.04 M_\odot$              |
| Companion mass                                     | $0.13 \pm 0.04 M_\odot$              | $0.10 \pm 0.02 M_\odot$              |
| Distance to the lens                               | $3.11 \pm 0.57$ kpc                  | $2.74 \pm 0.45$ kpc                  |
| Projected separation                               | $1.57 \pm 0.29$ AU                   | $1.38 \pm 0.23$ AU                   |
| Geocentric lens-source proper motion               | $5.42 \pm 0.39$ mas yr <sup>-1</sup> | $5.39 \pm 0.39$ mas yr <sup>-1</sup> |
| Heliocentric lens-source proper motion (north)     | $0.91 \pm 0.07$ mas yr <sup>-1</sup> | $1.58 \pm 0.11$ mas yr <sup>-1</sup> |
| Heliocentric lens-source proper motion (east)      | $6.43 \pm 0.47$ mas yr <sup>-1</sup> | $6.46 \pm 0.46$ mas yr <sup>-1</sup> |
| Ratio of the projected kinetic to potential energy | 0.04                                 | 0.02                                 |

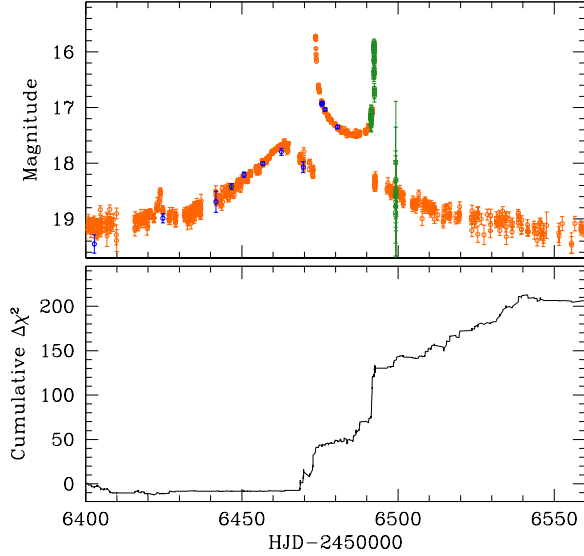


FIG. 5.— Cumulative distribution of  $\Delta\chi^2$  between the 2-body and 3-body models as a function of time.

the projected separation between the binary components and the geocentric lens-source proper motion are estimated by

$$a_\perp = sD_L\theta_E \quad (2)$$

and

$$\mu_\oplus = \frac{\theta_E}{t_E}, \quad (3)$$

respectively. We note that the geocentric reference frame is set with respect to the Earth position at  $t_0$  (HJD  $\sim 2456486$ ), which approximately corresponds to the time of the source star's closest approach to the center of mass of the binary lens. The heliocentric proper motion is estimated from the geocentric proper motion by

$$\boldsymbol{\mu}_\odot = \boldsymbol{\mu}_\oplus \frac{\pi_E}{\pi_E} + \frac{\mathbf{v}_{\oplus,\perp}}{\text{AU}} \pi_{\text{rel}}, \quad (4)$$

where  $\mathbf{v}_{\oplus,\perp} = (-2.1, 26.3)$  km s<sup>-1</sup> is the velocity of the Earth projected on the sky at the reference time, i.e.  $t_0$ . We also present ratio of the projected kinetic to potential energy (Dong et al. 2009) that is computed by

$$\left(\frac{\text{KE}}{\text{PE}}\right)_\perp = \frac{(r_\perp/\text{AU})^2}{8\pi^2(M_{\text{tot}}/M_\odot)} \left[ \left(\frac{1}{s} \frac{ds}{dt}\right)^2 + \left(\frac{d\alpha}{dt}\right)^2 \right]. \quad (5)$$

To be a bound system, the ratio of the binary lens should follow  $(\text{KE}/\text{PE})_\perp \leq \text{KE}/\text{PE} \leq 1$ . For both the  $u_0 > 0$  and  $u_0 < 0$  solutions, this condition is satisfied.

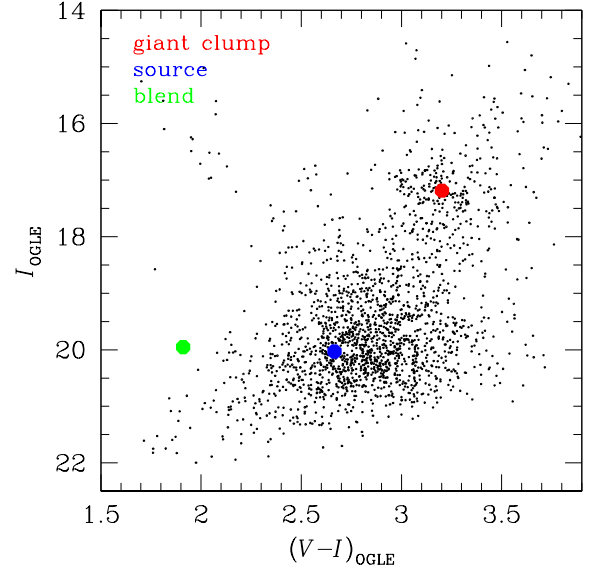


FIG. 6.— Positions of the source star and the blend with respect to the centroid of the giant clump in the color-magnitude diagram. The magnitude and color are calibrated to the OGLE-IV photometry.

The characteristics of the lens determined in the new analysis is greatly different from those determined in the previous analysis. The newly estimated masses of the binary components are  $M_1 \sim 0.2 M_\odot$  and  $M_2 \sim 0.1 M_\odot$ , indicating that they are low-mass stars, which are the most common population of Galactic lenses. On the other hand, the previous analysis characterized the lens system as a 3-body system where a terrestrial planet is orbiting sub-stellar brown-dwarf host accompanied by a low-mass companion. The distance to the lens estimated in the new analysis is  $D_L \sim 3$  kpc, which corresponds to roughly a halfway distance between the observer and the source and thus the lensing probability is maximized. By contrast, the previous analysis estimated a very close lens distance of  $D_L \lesssim 500$  for which the lensing probability is low. Therefore, the likelihood of the new interpretation is further supported by the fact that the physical parameters of the lens system correspond to the most probable values predicted by the mass function and distribution of Galactic matter.

## 5. SUMMARY

We presented a new interpretation of the microlensing event OGLE-2013-BLG-0723 that had been previously interpreted as a 3-body lensing event produced by a Venus-mass planet orbiting a brown-dwarf host in a binary system. The new solution, where the lens is composed of 2 bodies, can explain all anomalous features in the lensing light curve without the need to introduce an additional planetary companion. The fact that

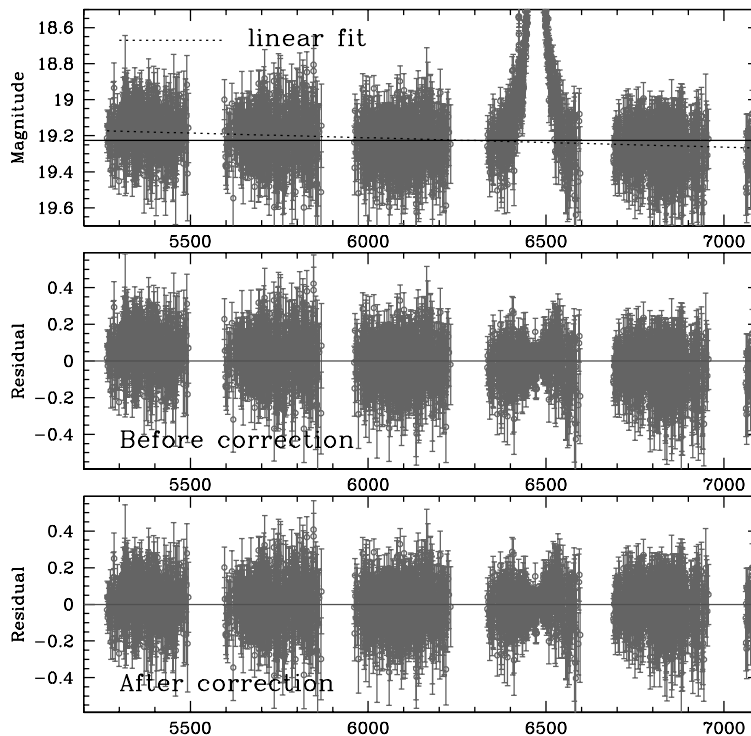


FIG. 7.— Systematic trend in the baseline flux (upper panel) and the procedure to correct the trend.

the new solution better explains the observed light curve than the previous solution with a simpler model implies that the new model is preferred, a conclusion that is also supported by Occam's razor. In addition, the fact that the physical parameters estimated from the new solution correspond to those of the most common lens population located at a distance of a large lensing probability further supports the likelihood of the new interpretation. Considering that two dramatically different solutions can explain the observed light curve, the event suggests the need of carefully testing all possible lens-system geometries. In particular, care must be taken to ensure that close binary solutions with caustic motion due to orbital

motion are considered. OGLE-2013-BLG-0723 is the second close stellar binary microlensing event that was originally misinterpreted as a binary star system with a planet.

Work by C. Han was supported by Creative Research Initiative Program (2009-0081561) of National Research Foundation of Korea. D.P.B. was supported by grants NASA-NNX13AF64G and NNX15AJ76G. The OGLE project has received funding from the National Science Centre, Poland, grant MAESTRO 2014/14/A/ST9/00121 to AU.

#### APPENDIX

##### CORRECTION OF BASELINE VARIATION

The light curve of OGLE-2013-BLG-0723 shows a systematic decline in the baseline. See the upper panel of Figure 7. A similar long term linear trend (of opposite sign) was seen in OGLE-2013-BLG-0341 and was eventually traced to a nearby bright star that was gradually moving toward (in that case) the source star, so that more of its flux was being "captured" in the tapered aperture used to estimate the source flux. We searched for such a moving bright star by examining the difference of two images, from 2004 and 2012. We indeed find a dipole from a bright star roughly 1.5" away, which is the characteristic signature of such moving stars. Having identified the cause of this trend, we conduct a linear fit for it and remove it. In the middle and lower panels of Figure 7, we present the baseline of the source star before and after the correction, respectively.

#### REFERENCES

- Albrow, M. D., Beaulieu, J.-P., Caldwell, J. A. R., et al. 2000, *ApJ*, 534, 894  
 Bennett, D.P. 2010, *ApJ*, 716, 1408  
 Bennett, D. P., Rhie, S. H., Becker, A. C., et al. 1999, *Natur*, 402, 57  
 Bessell, M. S., & Brett, J. M. 1988, *PASP*, 100, 1134  
 Claret, A. 2000, *A&A*, 363, 1081  
 Dominik, M. 1999, *A&A*, 341, 943  
 Dong, S., Gould, A., Udalski, A., et al. 2009, *ApJ*, 695, 970  
 Dong, Subo, DePoy, D. L., Gaudi, B. S., et al. 2006, *ApJ*, 642, 842  
 Gould, A. 1992, *ApJ*, 392, 442  
 Gould, A. 2000, *ApJ*, 542, 785  
 Griest, K., & Safizadeh, N. 1998, *ApJ*, 500, 37  
 Jung, Y. K., Han, C., Gould, A., & Maoz, D. 2013, *ApJ*, 768, L7  
 Jung, Y. K., Udalski, A., Sumi, T., et al. 2015, *ApJ*, 798, 123  
 Kervella, P., Bersier, D., Mourard, D., et al. 2004, *A&A*, 428, 587  
 Park, H., Udalski, A., Han, C., et al. 2013, *ApJ*, 778, 134  
 Skowron, J., Udalski, A., Gould, A., et al. 2011, *ApJ*, 738, 87  
 Udalski, A., Jung, Y. K., Han, C., et al. 2015, *ApJ*, 812, 47  
 Yoo, J., DePoy, D. L., Gal-Yam, A., et al. 2004, *ApJ*, 603, 139